Exploring the sintering behavior of a complex ceramic powder system using in-situ X-ray nano-tomography

Aatreya Manjulagiri Venkatesh, Roberto Barbano, Didier Bouvard, Pierre Lhuissier, Julie Villanova, Luis Olmos

▶ **To cite this version:**

Aatreya Manjulagiri Venkatesh, Roberto Barbano, Didier Bouvard, Pierre Lhuissier, Julie Villanova, et al.. Exploring the sintering behavior of a complex ceramic powder system using in-situ X-ray nano-tomography. Journal of the European Ceramic Society, 2024, 44 (12), pp.7236-7245. 10.1016/j.jeurceramsoc.2024.05.027 . hal-04596578

HAL Id: hal-04596578
https://hal.science/hal-04596578v1

Submitted on 31 May 2024

HAL is a multi-disciplinary open access archive for the deposit and dissemination of scientific research documents, whether they are published or not. The documents may come from teaching and research institutions in France or abroad, or from public or private research centers.

L'archive ouverte pluridisciplinaire **HAL**, est destinée au dépôt et à la diffusion de documents scientifiques de niveau recherche, publiés ou non, émanant des établissements d'enseignement et de recherche français ou étrangers, des laboratoires publics ou privés.

Exploring the sintering behavior of a complex ceramic powder system using in-situ X-ray nano-tomography

Aatreya Manjulagiri Venkatesh [a], Roberto Barbano [b], Didier Bouvard [c], Pierre Lhuissier [d], Julie Villanova [e], Luis Olmos [f]

[a] Univ. Grenoble Alpes, CNRS, Grenoble INP, SIMAP, 38000 Grenoble, France, mvaatreya@gmail.com

[b] Università degli Studi di Salerno, Via Ponte Don Melillo, I-84084 Fisciano (SA), Italy, robertobarbano25@outlook.it

[c] Univ. Grenoble Alpes, CNRS, Grenoble INP, SIMAP, 38000 Grenoble, France, didier.bouvard@grenoble-inp.fr

[d] Univ. Grenoble Alpes, CNRS, Grenoble INP, SIMAP, 38000 Grenoble, France, pierre.lhuissier@simap.grenoble-inp.fr

[e] ESRF - The European Synchrotron, 71 Avenue des Martyrs, 38000 Grenoble, France, julie.villanova@esrf.fr

[f] Universidad Michoacana de San Nicolás de Hidalgo, Morelia, Mexico, luisra24@gmail.com

Abstract

As a typical example of constrained sintering, the behavior of a complex ceramic powder system with multi-heterogeneities has been investigated. This powder system comprises inherent imperfections as well as rigid inclusions that act as constraints to densification. The sintering process of the system was monitored by in-situ X-ray nano-tomography at the European Synchrotron Radiation Facility (ESRF). This technique enables three-dimensional (3D) imaging of the microstructure with a voxel size of 25 nm. The images obtained reveal the distribution of imperfections in the powder system, such as particle aggregation and pore segregation in and around them. The subsequent in-situ evaluations show the evolution of the microstructure in the presence of inclusions. The study addresses the questions pertaining to the effect of the added constraints, the consequent crack generation and their implication on the final densification of the material.

Keywords

Ceramic nanopowders; Constrained sintering; Rigid inclusions; Synchrotron X-ray nano-tomography; In-situ investigation, Crack growth.

1 Introduction

A current trend in ceramic processing is the usage of ultra-fine powders (with a size of a few tens of nano-meters), which have attracted growing interest due to their superior properties and functionalities. An intrinsic feature of such nanopowders, however, is the presence of inhomogeneities at various stages of powder preparation and compaction. Particle features (shape, size distribution, agglomeration, defects) arising from the synthesis method, the forming conditions etc. can all contribute to these inhomogeneities. These inhomogeneities strongly affect the sintering behavior and the quality and performance of the final product. To overcome these concerns, it is essential to have a thorough understanding of the microstructural evolution and the mechanisms involved in the inhomogeneous sintering of nanopowders.

Several studies have investigated these topics and reported various observations and recommendations. For example, inhomogeneities, according to Exner [1], can appear as voids, as regions of non-uniform particle packing, and as agglomerates. Dynys *et al.* [2] confirmed that the densification rate decreases with increasing agglomerate content and provided a model to describe the densification kinetics. Lange [3] reported on the poor *sinterability* of agglomerated powder systems. Rhodes [4] emphasized the need to get rid of agglomerations to achieve the full potential of fine powders. Suggestions for reducing or eliminating inhomogeneities were stated in [5]. Furthermore, Evans [6] noted that the compact inhomogeneity must induce non-uniform sintering rates. Hsueh [7] explained that heterogeneities sinter at rates different than that of the host matrix and generate stresses that could lead to damage.

The complexity of the problem increases further when dealing with multicomponent systems, with high technological importance - such as composites, layered structures and materials containing rigid inclusions. Such systems undergo *constrained sintering* with mismatched shrinkage behavior [8]. Bordia *et al.* [9] provided a comprehensive review of the mechanisms and models for constrained sintering, as well as discussed the practical problems and applications of complex ceramic systems. They highlighted the need for improved understanding and control of the microstructural evolution and stress development during sintering with constraints. Sintering behavior in the case of constrained thin ceramic films are documented and numerical approaches capable of capturing the induced defects are detailed in Guillon *et al*. [10], [11].

However, most of the existing literature on this topic lacks high-resolution experimental images of the microstructural evolution during sintering. The studies are limited to low-resolution and/or ex-situ observations, which are unable to capture the dynamic changes in the microstructure brought on by the presence of constraints. Weiser *et al.* [12] studied the impact of inert particulates on the sintering kinetics of ceramic powders. They found that the presence of non-sintering inclusions reduced the densification rate of the ceramic matrix. Similar behavior was seen with zinc oxide powder compacts containing silicon carbide (SiC) particles in [13]. Lately, Okuma *et al.*, using synchrotron X-ray nano-tomography in their successive works, managed to capture the three-dimensional (3D) morphology of the defects in ceramic sintering and the overall evolution in multi-layer ceramic capacitors [14], [15]. Likewise, more experimental evidence in this regard could in fact help optimize the sintering of ceramic nanopowders with constraints. In their review article, Green *et al.* [16] indeed hypothesized that future advances in in-situ tomography techniques would make it possible to comprehend and tackle these issues better. In line with this suggestion, we utilize the recent developments in the science of synchrotron tomography to investigate the sintering of an industrial ceramic powder system at an unprecedented resolution scale.

Our research group has recently demonstrated the feasibility of using synchrotron X-ray nano-tomography (nano-CT) with a voxel size as low as 25 nm to observe the sintering of ceramic powders at high temperatures [17], [18]. We applied this technique to a model alumina powder and obtained successful post-mortem and in-situ observations of the densification and grain growth phenomena.

Here, we extend the nano-CT application to a ceramic system that is more complex and realistic, consisting of a ZnO nanopowder with inherent inhomogeneities. The sintering behavior of the powder system is monitored up to 1000°C, with and without inert alumina inclusions added into the ZnO matrix. The effect of the added inclusions on the ZnO microstructure and on the sintering behavior overall is explored. Qualitative descriptions of each stage of the in-situ observation are provided and the assertions are supported by clear visualizations.

2 Materials and methods

2.1 Powder system and sample preparation

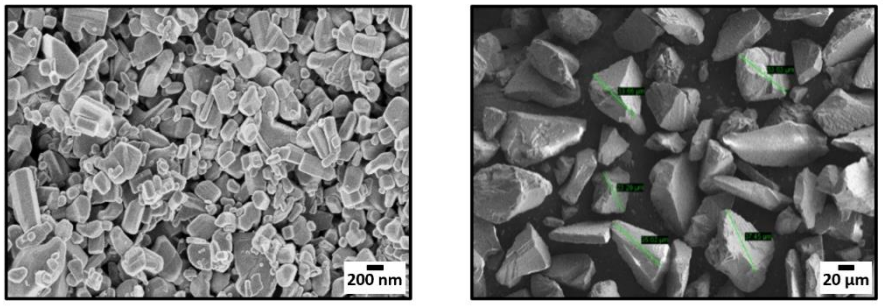

Figure 1. SEM observation of (a) ZnO powder with particle sizes of around 200 nm and (b) Al_2O_3 powder of around 22 µm, respectively.

The two powders employed in this study are a sub-micronic zinc oxide (ZnO) powder (average size of 200 nm, from CARLO ERBA GmbH) and an alumina (Al_2O_3) powder (average size of 22 µm, ~100 times larger than the ZnO particles). The scanning electron microscopy (SEM) images of both are given in **Figure 1**. ZnO nanoparticles comprise a variety of shapes such as prismatic, cuboid-like, thin rod-like, and other irregular profiles, while the Al_2O_3 particles are angular, with sharp corners and jagged edges.

For the experiments without alumina inclusions, the ZnO powder was mixed and pressed to shape uniaxially in a die under a pressure of ~60MPa. A small amount of stearic acid mixed with acetone was used as a lubricant for the die. The pressure was selected to ensure that the final compact density came up to around ~52%.

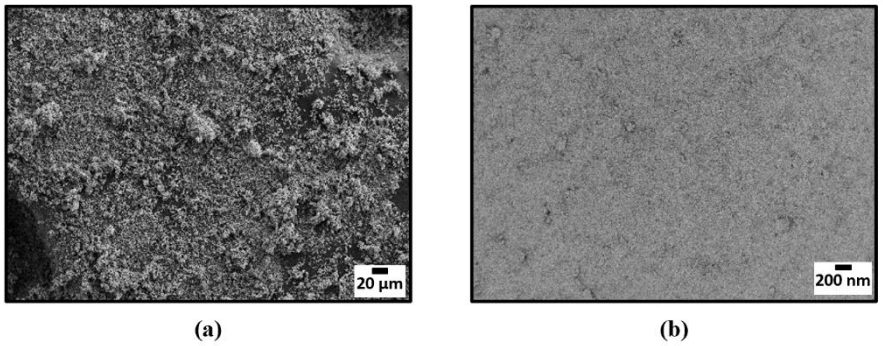

Figure 2. SEM observation of the ZnO powder (a) before and (b) after compaction.

Another SEM image, now with a lower magnification, indicates the presence of different types of entities (**Figure 2** (a)), prior to compaction, in the original ZnO powder. The inherent heterogeneities are visible - nanoparticles tend to stick together due to their higher surface energy and area, forming agglomerates. The compaction process (**Figure 2** (b)) reduces the overall porosity and causes most of the *softer* agglomerates to disintegrate. There are still, however, regions with larger porosity, due to the fact that the *harder* agglomerates, which are resistant to breakage, remain intact. These are referred to as *aggregates* in this study. They have a size range of up to several tens of microns. There are also other *larger elements* that originate from the processing route. These elements are also a few microns in size. They cannot be clearly distinguished from the aggregates with the SEM images but will be better identified by tomography images in the later sections.

For the experiments with inclusions, 20 vol % of alumina particles are mixed together with the ZnO powder to form a composite. This blend is compacted following the same procedure as above. The relative density of the compacts read ~50%.

2.2 Dilatometry experiments

Preliminary dilatometry experiments were conducted in *SETARAM's SETSYS Evolution - 1750 CS* to trace the sintering behavior, with and without alumina inclusions (**Figure 3**). With a heating rate of 5°C/min and an original relative density of ~52%, the change in shrinkage of the compact was measured as a function of time from the room temperature to 1000°C. At 1000°C, the experiment without alumina inclusions shrunk the compact by ~16%. Final relative density calculated by the Archimedes approach read ~92%. However, with 20% alumina inclusions, following the same thermal cycle, the density attained was significantly limited (~77%), causing a shrinkage of only ~12%. This signals that the addition of inclusions hampered the densification process. The underlying mechanisms for this drastic difference in density and shrinkage will be deciphered later with the tomography analyses.

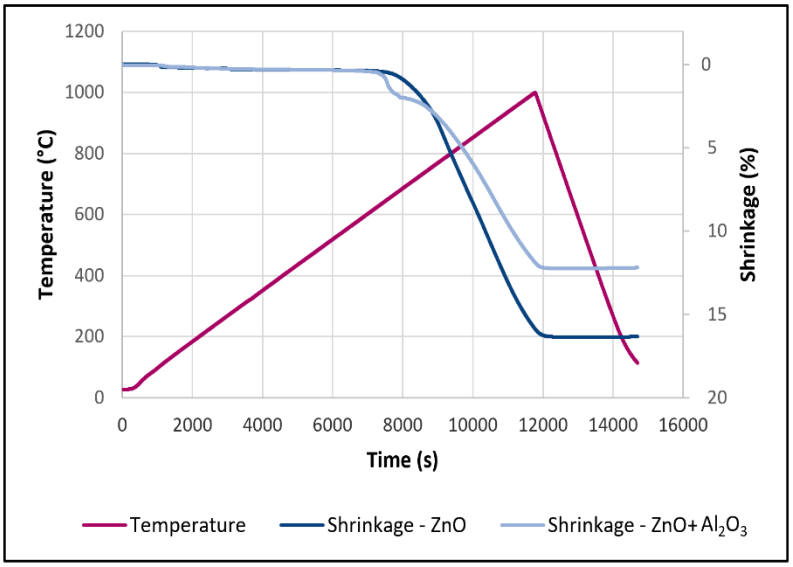

Figure 3. Dilatometry curves showing the trajectory of the shrinkage in the compact, with and without alumina inclusions.

2.3 X-ray nano-tomography experiments

For the samples without alumina inclusions, we performed post-mortem experiments [17] by scanning the samples that have already been subjected to the sintering cycle in the dilatometer. For the sample with alumina inclusions, interrupted in-situ experimentations were carried out inside the synchrotron hutch [18], by scanning the same region of the sample during the heat treatment, capturing the sintering evolution. We followed the same phase-contrast experimental set-up and procedure as described in our previous works [17] [18] (except for the furnace, described below). This technique has a proven record of attaining higher resolutions. In addition, the difference between the two 'phases' of ZnO and Al_2O_3 here in terms of their very different absorption coefficients could be exploited as well. For post-mortem, the sintered compacts were broken into smaller fragments. For in-situ, the *green* compact obtained just after compaction was broken. We expect this operation to not introduce significant damage in the material. The fragments are ~100 µm in diameter and ~1-2 mm in height in both the cases, suitable for nano-CT experiments at the ESRF synchrotron.

Holotomography (4-distance imaging) involved a total of 3203 projections over a full rotation, collected using an X-ray beam with an energy of 29.1keV for each tomographic scan [19]. The resulting 3D volume of 64*64*54 μm^3 presents a voxel size of 25nm. 3D reconstructed images of the internal structure of the compacts were obtained at five different sintering temperatures: room, 800°C, 900°C, 1000°C, and 1000°C + 30 min of isothermal holding.

A built-in furnace of the ESRF with a Ni-Cr resistor, clad in an Inconel shell, was used for these real-time assessments [20]. The ZnO sample was subjected to temperature ramps as the furnace descended on it. The furnace was made to move out from the sample once it reached the desired temperatures, to execute the 4-distance imaging process, which took about 20 min. It is anticipated that the microstructure would remain frozen during this time. An iterative Paganin-based method with a delta over beta value of 59.7 was chosen to perform the phase retrieval of radiographs [21], and ESRF's PyHST2 software package was then used for the subsequent reconstruction, to obtain the 3D volumes of the samples [22].

3 Results

3.1 Post-mortem investigation

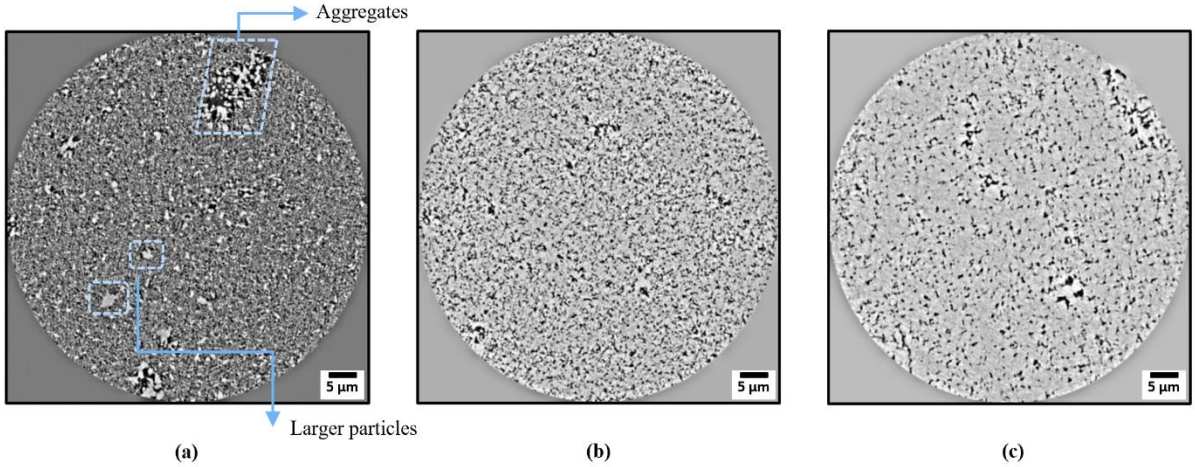

Figure 4. Cross-section slices extracted from the 3D reconstructed volumes for ZnO samples at (a) the green state, and observed post-mortem after sintering at (b) 800°C and (c) 1000°C, respectively.

First, we present the results obtained from the post-mortem nano-CT of the ZnO powder compacts. **Figure 4** (a) shows the microstructure of the ZnO powder at the green state, before sintering, and with no alumina inclusions. In the figure, the ZnO matrix is in shades of gray, while the black phase is porosity. The material is porous with a relative density of ~52%, as evidenced by the pore spaces in the image. The resolution of the imaging, although not effective enough to view the individual particles, is good enough to detect the inhomogeneities (spaces with higher porosity) present in the powder packing. As a consequence of the particle aggregation, the particles have a wide size distribution, and some regions have higher porosity

than others. It is possible here to make a distinction between the *aggregates* and the so-called *larger ZnO particles*.

The microstructure of the compact after sintering at 800°C is depicted in **Figure 4** (b). The image shows the process of densification, together with some grain growth that has occurred during sintering, making the grains clearly distinguishable from the pores now. Nonetheless, a distribution of porosity still seems to exist. At 1000°C, in **Figure 4** (c), prevailing massive grain growth can be observed, with a much higher densification of the material. The density of the compact reaches ~92%, corresponding to the 16% shrinkage that was earlier noted via the dilatometry experiment. Two classes of porosity can be noticed, with smaller pores that have gradually shrunk and the larger pore segregations that are visible in a few locations here and there. These three figures show more or less the expected course of action that is bound to happen during a sintering process. This is taken as a reference for the subsequent in-situ imaging carried out on the sintering of the same microstructure but with additional larger alumina inclusions inside.

3.2 In-situ investigation

A global view of the powder system at the green state is displayed in **Figure 5**, obtained after the 3D reconstructions of the in-situ observations.

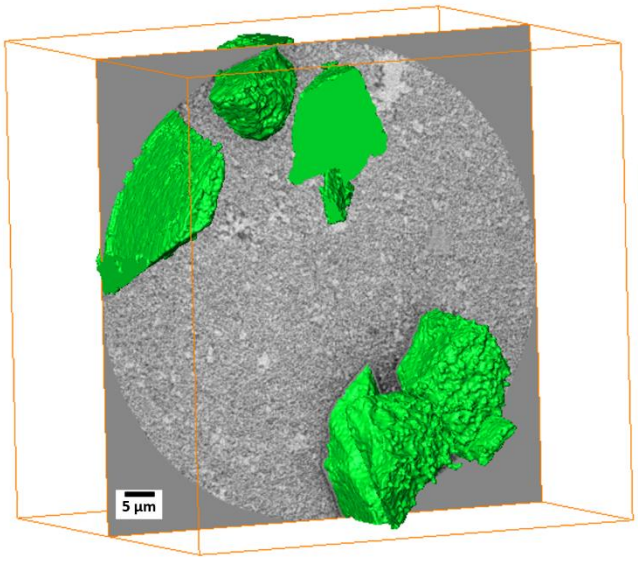

Figure 5. An overview of the material system under consideration, showing one of the slices of the image stack (64*64*54 µm3) with the ZnO matrix and the alumina inclusions in green in 3D.

From here on in this study, for the sake of convenience, the 3D image stacks are categorized into two regions based on their proximity to the added alumina inclusions - *Region 1* referring to the areas that are far from the inclusions, and *Region 2* in the vicinity of inclusions (**Figure 6**).

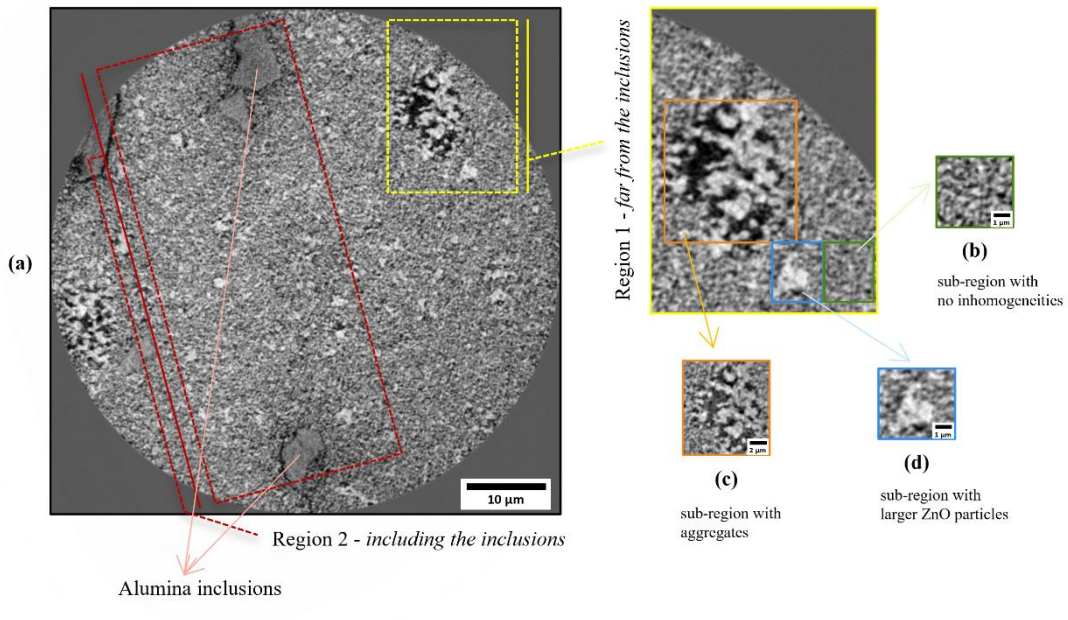

Figure 6. (a) One of the slices of the image stack (taken from mid-volume) depicting the categorization of the images into regions far from the alumina inclusions (Region 1) and regions including the alumina inclusions (Region 2). (b), (c), (d) show the sub-regions with no apparent inhomogeneities, aggregates and larger ZnO particles respectively.

Microstructure evolution far from the alumina inclusions

The idea of analyzing Region 1 separately is to check the behavior of the regions away from the influence of the alumina inclusions, so as to regard them as regions supposedly undergoing *free sintering* and capture their evolution over time. In this context, it entails taking a look at the effect of the inhomogeneities prevalent in the ZnO matrix on the microstructure, without the added impact of the inclusions. Of course, this does not necessarily imply that the regions in question would be totally unaffected by the inclusions, but it is presumed to be minimal. These regions are selected based on a careful distance mapping, so that the inclusions are not in sight for a minimum number of voxels (~500) in the X and the Y-direction, and for at least 500 slices in the Z-direction.

Furthermore, Region 1 is divided into 3 more distinct sub-regions, to try and encompass the variability in the ZnO matrix – Sub-regions with only the ZnO matrix, Sub-regions with ZnO

matrix and aggregates, and sub-regions with ZnO matrix and larger ZnO particles. We compare and discuss the different sintering behaviors exhibited by these regions depending upon the presence and the type of inhomogeneities. One such representative region for each of the cases mentioned is displayed in the **Figure 6** (b) (c) (d) and taken in for the discussion below.

The in-situ observation of the sub-region 1 with only the ZnO matrix (**Figure 6** (b)) at different times shows a typical sintering behavior, as seen from **Figure 7**. Sintering in the absence of strong particle aggregation as such is expected to allow the attainment of higher densification rates than for sintering with aggregation. These sub-regions have the highest packing density in the matrix and therefore should see the most rapid densification. Likewise, the individual particles in **Figure 7** (a), with uniform and homogeneous microstructure tend to enhance the sintering progression. The grain packing appears to gradually densify from the room temperature up until 900°C, and the pores in the matrix shrink during the process (**Figure 7** (a) (b) (c)). Later, the particles increasingly merge and grow in size (**Figure 7** (d) (e)). As a likely consequence of this grain growth, pore coalescence can be noticed towards the end, especially during the period of isothermal holding (**Figure 7** (e)).

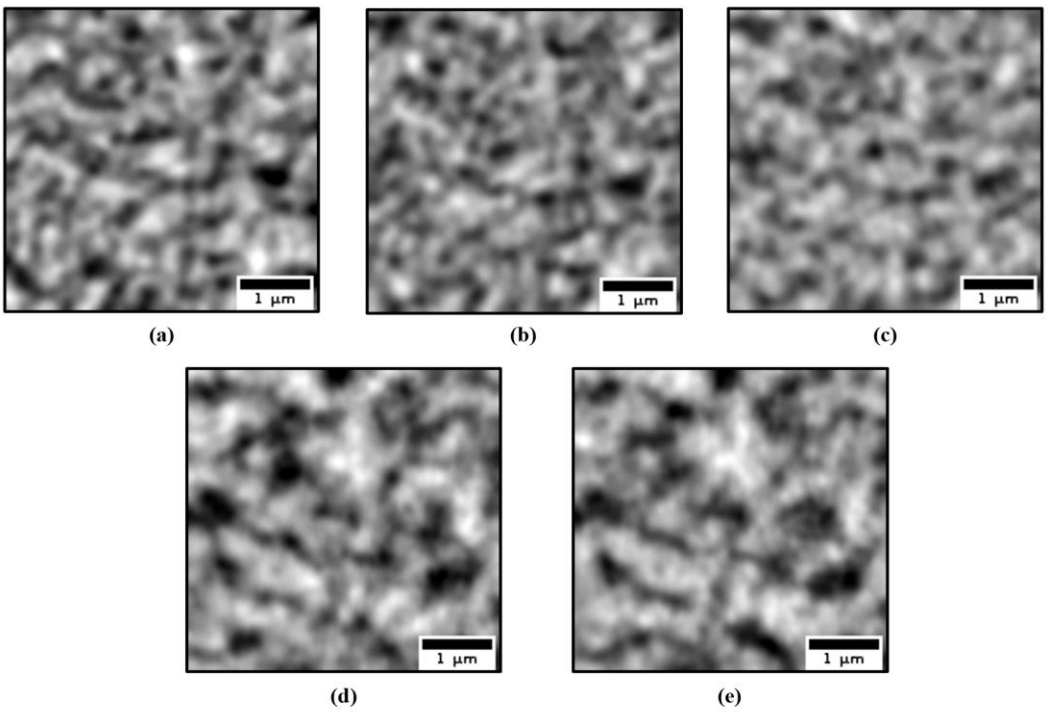

Figure 7. Follow-up of the in-situ observation of one of the sub-regions with only the 3D reconstructed ZnO matrix at (a) room temperature, (b) 800°C, (c) 900°C, (d) 1000°C, and (e) 1000°C + 30 min of isothermal holding, respectively.

The following paragraphs discuss the sub-regions 2 in Region 1, which contribute to the non-uniformity in the powder system.

The sub-region with aggregates (**Figure 6** (c)) includes strongly bonded clusters of smaller particles that resist disintegration during powder compaction. These aggregates create heterogeneous packing in the green body, which leads to differential sintering of the compact [23]. Moreover, the lower packing density here has an adverse effect on the *sinterability* and limits the density of the final product.

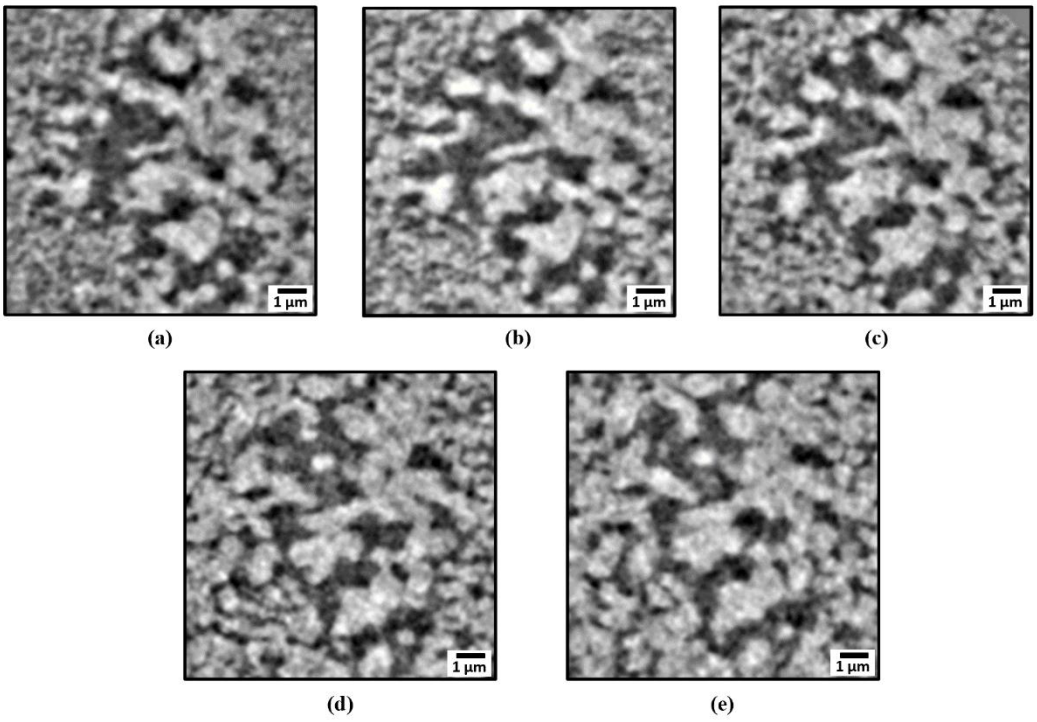

Figure 8. Follow-up of the in-situ observation of one of the sub-regions with aggregates in the 3D reconstructed ZnO matrix at (a) room temperature, (b) 800°C, (c) 900°C, (d) 1000°C, and (e) 1000°C + 30 min of isothermal holding, respectively.

Figure 8 shows the in-situ observation of the aggregates' behavior during sintering. It shows a starkly different conduct from the previous sub-region. Initially, in **Figure 8** (a), the aggregates are poorly connected to the matrix particles and are surrounded by pores. Further, throughout the sintering process, the aggregates change slightly over time, but they do not break or deform significantly. The pores around remain mostly stable and intact. However, all around the aggregates, we see grain growth occurring in the matrix over time.

Additionally, the original powder contains some ZnO particles that are larger and more irregular than the rest of the matrix. These particles are considered in the sub-region 3 (**Figure**

6 (d)). They do not break on compaction and are anticipated to show complex and varied sintering behavior. Salehi *et al.* [24] reported that such larger particles have a negative effect on the packing density and the homogeneity of the matrix.

The larger particles also possess isolated large pores in and around them (**Figure 9** (a)). These *heteropores* could be attributed to the poor packing of the smaller particles around the larger ones during compaction, as reported by Jonghe *et al.* [25]. They are not easily eliminated during sintering, as they are weakly connected to the surrounding matrix and thus have a low driving force for sintering [26]. Porras *et al.* [27] studied the stability and redistribution of such related pores and found that they can exhibit complex and different behaviors depending on their location and size.

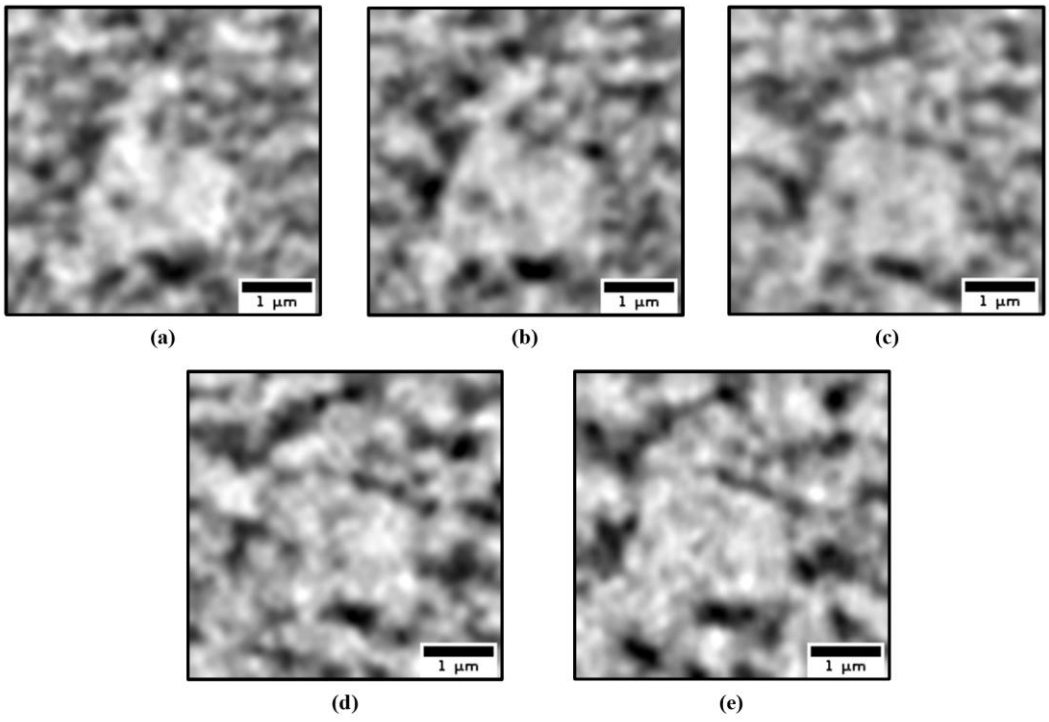

Figure 9. Follow-up of the in-situ observation of one of the sub-regions with larger particles in the 3D reconstructed ZnO matrix at (a) room temperature, (b) 800°C, (c) 900°C, (d) 1000°C, and (e) 1000°C + 30 min of isothermal holding, respectively.

During sintering, as seen from the set of images (**Figure 9**), the larger particles behave more rigidly than the aggregates. They retain their core shape, but merge with other grains over time, forming an even larger version of the same. The pore evolution (from **Figure 9** (b) onwards) is complex and varied along the surface of the larger particles. Some pores around the particles stay the same, while others increase in size due to the coalescence of smaller pores around them. In addition, we find that some of the larger particles contained *intra-pores* that vanished during sintering, indicating a densification process within the particles. This is because the

smaller pores have a higher surface area and curvature, which makes them more prone to shrinkage. The larger pores, on the other hand, have a lower specific surface area and curvature, which makes them more resistant to the same [28], [29].

On the whole, the sintering characteristics of the compact would deteriorate due to the low-sintering characteristics of the aggregates and the much coarser particles, and the slow shrinkage of the larger pores, resulting in a more porous and a weaker product. The imperfections here in the in-situ observation do not appear to collapse easily, but instead persist and create further complications. This behavior is in contrast to the post-mortem image sequence in **Figure 4**. No significant densification is observed in the sub-regions with the imperfections, indicating that it can contribute to the hindering of the sintering process of the overall matrix, and thereby reduce the strength of the sintered material. This essentially suggests the wide-ranging impact of the alumina inclusions (discussed further in the subsequent section) even at distant locations from their positions.

Microstructure evolution in the vicinity of the alumina inclusions

Moving on to the second region in the study - Region 2, and focusing our attention on the role of the alumina inclusions in the ZnO matrix. The region contains a network of deliberately introduced much coarser alumina particles (average size of 22 µm), into the matrix ((**Figure 5**) (**Figure 6** (a))), setting up a *constrained sintering* framework. This is likely to create a higher degree of inhomogeneity in the microstructure, the extent of which is analyzed in this section.

The alumina particles behave as rigid inert inclusions, as they do not deform or react with the surrounding ZnO matrix. Poor packing of the ZnO particles around the alumina inclusions generate voids adjacent to them from the very beginning (**Figure 10** (a)). In addition to poor initial packing, the action of unloading after die-pressing could also possibly be responsible for the defects around the inclusions. These voids at the matrix-inclusion interface, referred to by many terms in the literature, such as circumferential voids, peripheral pores etc. are responsible for the large suppression in the densification rate during the initial stages of sintering [30], [31], [32].

The formation of initial voids next to the inclusions is a common feature with respect to all the inclusions here in the system. As illustrated in **Figure 10** (a), over time, as sintering progresses, the voids become thicker and more pronounced, creating a strong density variation around the interface. Initiation of cracks can be seen in **Figure 10** (b) and **Figure 10** (c), which is further

clearly visible from 1000°C onwards (**Figure 10** (d)). In the neighboring matrix, significant grain growth can be seen over the course of sintering.

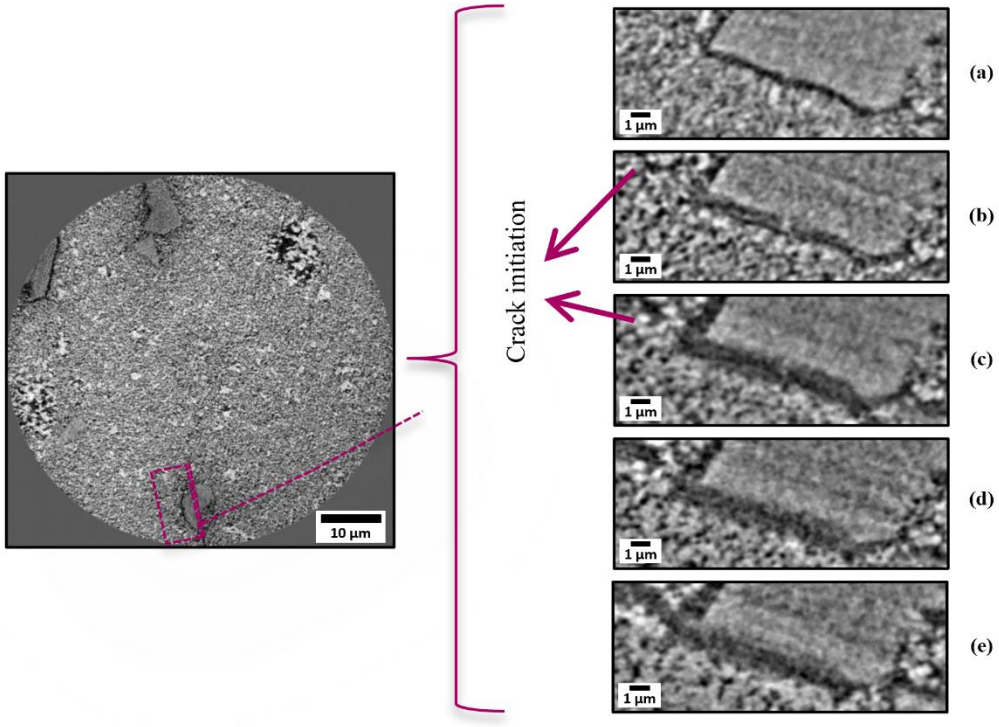

Figure 10. Follow-up of the voids generated at the matrix-inclusion interface at (a) room temperature, (b) 800°C, (c) 900°C, (d) 1000°C, and (e) 1000°C + 30 min of isothermal holding, respectively.

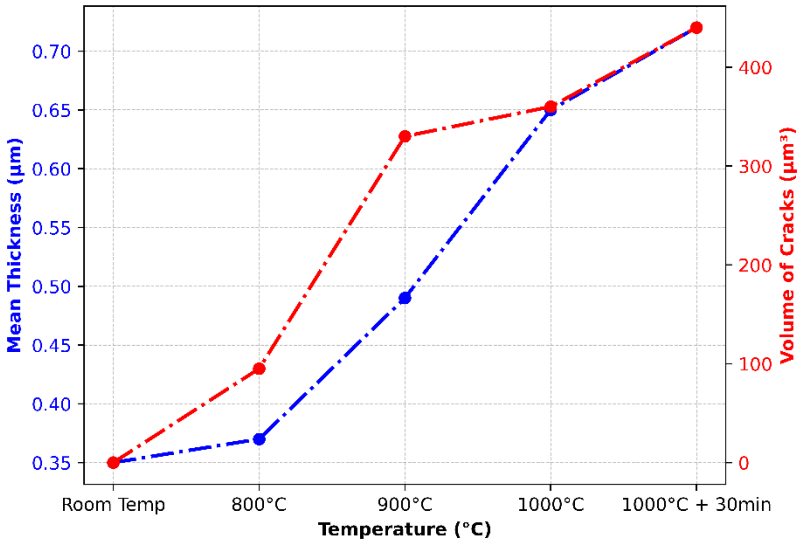

Figure 11. Evolution of thickness of the pores around alumina inclusions and the volume of the cracks at different temperature intervals.

This is reflected in a quantitative analysis performed using the BoneJ plugin in ImageJ software [33]. The analysis focused on the thickness distribution of all the pores surrounding the inclusion. The resulting mean thickness value has been incorporated into **Figure 11**, which demonstrates a continuous increase from 0.35 in the green state to ~0.7 µm at the end of sintering.

To know more on these crack-like defects, if they further open during sintering or just exist as imperfections, a wider view of the region is considered here. **Figure 12** is a tracker of the cracks taken from cross-section visualizations at various sintering temperatures. We find that the voids at the matrix-inclusion interface in fact act as pre-existing flaws. The extent of the cracks increases at every time-step, both in terms of their magnitude and severity. A 3D segmentation of the cracks and the subsequent volume calculation of their renderings compiled using the Avizo software [34] is plotted in **Figure 11**, with the volume of the crack increasing steadily as sintering progresses.

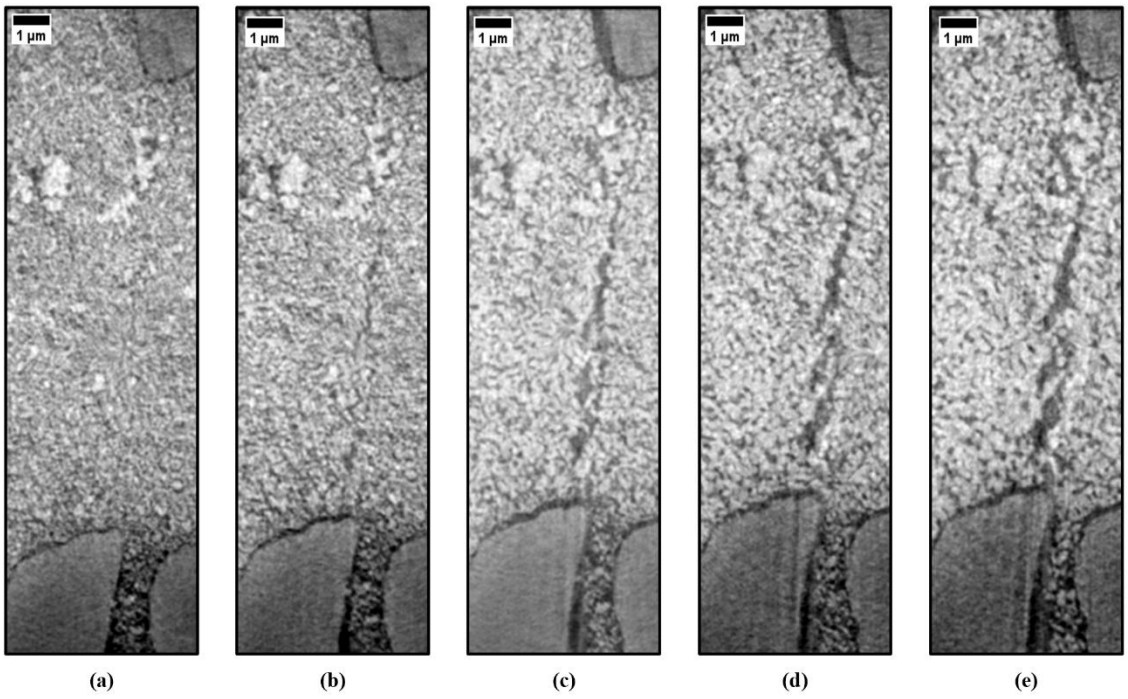

Figure 12. Follow-up of the crack initiation and propagation in between the alumina inclusions at (a) room temperature, (b) 800°C, (c) 900°C, (d) 1000°C, and (e) 1000°C + 30 min of isothermal holding, respectively.

As compiled in Bordia *et al*. [9] and as observed in Lange *et al*.'s works [35], [36] in the context of constrained sintering, the damage here indeed begins in the early stages of densification and near pre-existing defects/voids.

The reasons for the crack formation are anticipated to be the stresses generated as a result of the inclusions added to the system, as remarked in a few theoretical approaches [37], [38] and experimental studies [30], [39]. These stresses have been given an overall term 'back stresses' by Tuan et al. [31] and they are supposed to exist in the matrix, in the inclusions, and at the inclusion-matrix interface. According to these authors, these internal stresses can arise from an external constraint or from the differential densification due to inhomogeneities. We can rest assured that in the present study, the main source of internal stresses is the constraint imposed by the presence of inert alumina inclusions.

Our understanding is that the matrix space here can be thought of being divided into sub-domains partly surrounded by rigid-natured inclusions. Each of these sub-domains, which are expected to shrink during sintering, faces resistance by the hard-to-move inclusions, in what can be referred to as *constrained sintering*. Tensile stresses thus develop at the sub-domain interfaces, which are dotted with inclusions. As demonstrated in **Figure 12**, these stresses logically result in cracks, propagating from one inclusion to another, starting from the flaws already present around the inclusions, particularly from **Figure 12** (b) onwards. All the cracks in the entire volume were checked for the possible routes of propagation. This feature of crack initiation and propagation was observed consistently, and, once initiated, they were found to propagate through the 3D network of these inclusions.

Furthermore, it could also be inferred from **Figure 12** that the cracks, rather than being a mere linkage of pores, have a well-defined path. They also cause a separation of initially sintered grains in some cases. The impact of the inclusions becomes progressively more critical as the densification proceeds (**Figure 12** (d) (e)).

In all probability, these cracks would act as strength-limiting flaws and cause irreversible structural damage, proving fatal for the properties of the sintered parts. In addition, the fact that the presence of inclusions prevents the matrix regions away from the inclusions from sintering uniformly has already been established in the previous section.
The relative significance of the inclusion volume fraction, the inclusion size and of other processing conditions are beyond the scope of this study.

Overall, it is safe to declare that, together with the implications of the inherent inhomogeneities, the cracks due to the constraints are major contributors to the significantly lesser shrinkage observed in the powder system. This justifies the lesser final densification (~77%) attained in the dilatometry experiments for the inclusion-added system earlier. Also, the aggregates and

the larger ZnO particles behave rigidly, yes, but their impact is marginal in comparison to the effect of the rigidity of the alumina inclusions.

It is also to be noted that we attempted to conduct a more thorough quantitative analysis on the sintering evolution. However, the resolution of the images was not sufficient enough to detect the individual nanoparticles and pores accurately and the results were found not to be precise and reliable. Except for the most pronounced phenomena, such as the growth of pores around the inclusions and the propagation of cracks from one inclusion to another, it was therefore decided to focus on a qualitative account of the trends observed.

4 Conclusion

The sintering behavior of a ZnO-based powder compact with several heterogeneities has been visualized using nano-scale (25nm) imaging at the ESRF synchrotron.

The microstructure of the powder compact was compared with and without inclusions - by visualizing a post-mortem sample without inclusions and introducing the inclusions during the in-situ observation.

Post-mortem imaging at this scale was good enough to perceive the heterogeneities of the system and its evolution during sintering. The heterogeneities get effectively minimized over the course of sintering, leading to densification in the compact.

When additional larger alumina inclusions were added into the matrix, with in-situ imaging, it was found out that these inclusions have a clear impact on the sintering process. They have a significant effect on the microstructure not only in their immediate vicinity, but also far away from them. Real-time assessments of the system show the behavior of the inhomogeneities in the presence of inclusions such as the aggregates and the larger ZnO particles in the matrix, formation and persistence of large pores, and the ensuing spatial density variations.

Additionally, the inclusions are observed to be acting as rigid constraints inducing damage around it, which spreads into the surrounding matrix during sintering. The voids, initially present adjacent to the inclusions, were found to later manifest as cracks during sintering. Crack initiation and their progression afterwards were seen to be from one inclusion to another. These factors were seen to influence and lower the overall densification and shrinkage of the material system. The cracks are imagined to compromise the structural integrity and the properties of the sintered components.

Given further resolution-related improvements in the future, this work establishes a solid basis for a systematic quantitative study on the sintering of such nanoscale powders, both with or without constraints. Forthcoming efforts could make use of the nano-holotomography imaging system and the resolution attained to check the retarding effect of the inclusions in terms of their size, shape, number and spacing on the sintering kinetics and microstructure. Optimal sintering conditions for a given set of inclusions could be identified, and the possible scenarios if and when the added inclusions could be detrimental for the sintering process may be explored.

Acknowledgements

This project has received funding from the European Union's Horizon 2020 research and innovation programme under the Marie Skłodowska-Curie grant agreement MATHEGRAM No 813202. The authors also thank the ESRF for the provision of synchrotron radiation facilities (Proposal MA5301).

References

[1] H. E. Exner, "Principles of single-phase sintering," *Reviews on powder metallurgy and physical ceramics*,(1/4), pp. 1-251, 1979.

[2] F. W. Dynys and J. W. Halloran, "Influence of Aggregates on Sintering," *Journal of the American Ceramic Society*, vol. 67, no. 9, pp. 596–601, 1984, doi: 10.1111/j.1151-2916.1984.tb19601.x.

[3] F. F. Lange, "Sinterability of Agglomerated Powders," *Journal of the American Ceramic Society*, vol. 67, no. 2, pp. 83–89, 1984, doi: 10.1111/j.1151-2916.1984.tb09620.x.

[4] W. H. Rhodes, "Agglomerate and Particle Size Effects on Sintering Yttria-Stabilized Zirconia," *Journal of the American Ceramic Society*, vol. 64, no. 1, pp. 19–22, 1981, doi: 10.1111/j.1151-2916.1981.tb09552.x.

[5] F. F. Lange, "Powder Processing Science and Technology for Increased Reliability," *Journal of the American Ceramic Society*, vol. 72, no. 1, pp. 3–15, 1989, doi: 10.1111/j.1151-2916.1989.tb05945.x.

[6] A. G. Evans, "Considerations of Inhomogeneity Effects in Sintering," *Journal of the American Ceramic Society*, vol. 65, no. 10, pp. 497–501, 1982, doi: 10.1111/j.1151-2916.1982.tb10340.x.

[7] C.-H. Hsueh, “Sintering behaviour of powder compacts with multi heterogeneities,” *Journal of materials science*, vol. 21, pp. 2067-2072, 1986.

[8] F. Wakai, G. Okuma, and N. Nishiyama, “Sintering mechanics of ceramics: a short review,” *Materials Today: Proceedings*, vol. 16, pp. 4-13, 2019.

[9] R. K. Bordia, S. J. L. Kang, and E. A. Olevsky, “Current understanding and future research directions at the onset of the next century of sintering science and technology,” *Journal of the American Ceramic Society*, vol. 100, no. 6, pp. 2314–2352, Jun. 2017, doi: 10.1111/jace.14919.

[10] O. Guillon, E. Aulbach, J. Rödel, and R. K. Bordia, “Constrained sintering of alumina thin films: Comparison between experiment and modeling,” *Journal of the American Ceramic Society*, vol. 90, no. 6, pp. 1733–1737, 2007, doi: 10.1111/j.1551-2916.2007.01650.x.

[11] O. Guillon, R. K. Bordia, and C. L. Martin, “Sintering of thin films/constrained sintering,” *Sintering of Advanced Materials*, Elsevier, pp. 415–434e, 2010, doi: 10.1533/9781845699949.3.415.

[12] M. W. Weiser and L. C. De Jonghe, “Inclusion Size and Sintering of Composite Powders,” *Journal of the American Ceramic Society*, vol. 71, no. 3, p. C-125-C-127, 1988, doi: 10.1111/j.1151-2916.1988.tb05030.x.

[13] L. C. De Jonghe, M. N. Rahaman, and C. H. Hsueh, “Transient stresses in bimodal compacts during sintering,” *Acta Metallurgica*, vol. 34, no. 7, pp. 1467-1471, 1986.

[14] G. Okuma, S, Watanabe, K. Shinobe, N. Nishiyama, A. Takeuchi, K. Uesugi, S.Tanaka, and F. Wakai, “3D multiscale-imaging of processing-induced defects formed during sintering of hierarchical powder packings,” *Scientific reports*, vol. 9, no. 1, Dec. 2019, doi: 10.1038/s41598-019-48127-y.

[15] G. Okuma, N. Saito, K. Mizuno, Y. Iwazaki, R. Inoue, H. Kishi, A. Takeuchi, M. Uesugi, K. Uesugi, and F. Wakai, “Microstructural evolution of electrodes in sintering of multilayer ceramic capacitors (MLCC) observed by synchrotron X-ray nano-CT,” *Acta Materialia*, vol. 206, Mar. 2021, doi: 10.1016/j.actamat.2020.116605.

[16] D. J. Green, O. Guillon, and J. Rödel, “Constrained sintering: A delicate balance of scales,” *Journal of the European Ceramic Society*, vol. 28, no. 7, pp. 1451–1466, 2008, doi: 10.1016/j.jeurceramsoc.2007.12.012.

[17] A. M. Venkatesh, D. Bouvard, P. Lhuissier, and J. Villanova, “3D analysis of ceramic powder sintering by synchrotron X-ray nano-tomography,” *Journal of the European Ceramic Society*, vol. 43, no. 6, pp. 2553–2563, Jun. 2023, doi: 10.1016/j.jeurceramsoc.2022.12.065.

[18] A. M. Venkatesh, D. Bouvard, P. Lhuissier, J. Villanova and C. Rajon, “In-situ 3D X-ray investigation of ceramic powder sintering at the particle length-scale,” *Ceramics International*, 2023, doi: 10.1016/j.ceramint.2023.11.216

[19] P. Cloetens, W. Ludwig, J. Baruchel, D. V. Dyck, J. V. Landuyt, J. P. Guigay, and M. Schlenker, “Holotomography: Quantitative phase tomography with micrometer resolution using hard synchrotron radiation x rays,” *Applied Physics Letters*, vol. 75, no. 19, pp. 2912–2914, Nov. 1999, doi: 10.1063/1.125225.

[20] J. Villanova, R. Daudin, P. Lhuissier, D. Jauffres, S. Lou, C. L. Martin, S. Labouré, R. Tucoulou, G. Martínez-Criado, and L. Salvo, “Fast in situ 3D nanoimaging: a new tool for dynamic characterization in materials science,” *Materials Today*, vol. 20, no. 7, pp. 354–359, Sep. 2017, doi: 10.1016/j.mattod.2017.06.001.

[21] D. Paganin, “Coherent X-Ray Optics,” *Oxford University Press*, 2006.

[22] A. Mirone, E. Brun, E. Gouillart, P. Tafforeau, and J. Kieffer, “The PyHST2 hybrid distributed code for high speed tomographic reconstruction with iterative reconstruction and a priori knowledge capabilities,” *Nuclear Instruments and Methods in Physics Research Section B: Beam Interactions with Materials and Atoms*, vol. 324, pp. 41–48, Apr. 2014, doi: 10.1016/j.nimb.2013.09.030.

[23] T. -S. Yeh and M. D. Sacks, “Effect of Particle Size Distribution on the Sintering of Alumina,” *Journal of the American Ceramic Society*, vol. 71, no. 12, p. C-484-C-487, 1988, doi: 10.1111/j.1151-2916.1988.tb05812.x.

[24] A. Salehi, G. Pircheraghi, and R. Foudazi, “Pore structure evolution during sintering of HDPE particles,” *Polymer*, vol. 183, Nov. 2019, doi: 10.1016/j.polymer.2019.121865.

[25] L. C. De Jonghe, M.-Y. Chu, and M. K. F. Lin, “Pore size distribution, grain growth, and the sintering stress.” *Journal of Materials Science*, vol. 24, pp. 4403-4408, 1989.

[26] A. G. Evans and C. H. Hsueh, “Behavior of Large Pores During Sintering and Hot Isostatic Pressing,” *Journal of the American Ceramic Society*, vol. 69, no. 6, pp. 444–448, 1986, doi: 10.1111/j.1151-2916.1986.tb07442.x.

[27] F. Lorenzano-Porras, D. H. Reeder, M. J. Annen, P. W. Carr, and A. V Mccormick, "Unusual Sintering Behavior of Porous Chromatographic Zirconia Produced by Polymerization-Induced Colloid Aggregation," *Industrial & engineering chemistry research*, vol. 34, no. 8, pp. 2719–2727, 1995.

[28] R. M. German, "Coarsening in sintering: Grain shape distribution, grain size distribution, and grain growth kinetics in solid-pore systems," *Critical Reviews in Solid State and Materials Sciences*, vol. 35, no. 4, pp. 263–305, Oct. 2010, doi: 10.1080/10408436.2010.525197.

[29] J. A. Varela, O. J. Whittemore, and E. Longo, "Pore Size Evolution during Sintering of Ceramic Oxides," *Ceramics International*, vol. 16, no. 3, pp. 177-189, 1990.

[30] T. Kimura, H. Kajiyama, R. Yazaki, and T. Yamaguchi, "Effects of nondensifying inclusions on the densification and microstructure of zinc oxide matrix composites," *Journal of Materials Science*, vol. 31, pp. 4149-4157, 1996.

[31] W. H. Tuan, E. Gilbart, and R. J. Brook, "Sintering of heterogeneous ceramic compacts Part 1 AI203-AI203," *Journal of Materials Science*, vol. 24, pp. 1062-1068, 1989.

[32] S. M. Salamone, "Densification of and constitutive laws for ceramic matrix composites and multilayered systems - PhD Thesis," University of Washington, Seattle, 2003.

[33] Doube M, Kłosowski MM, Arganda-Carreras I, Cordelières FP, Dougherty RP, Jackson JS, Schmid B, Hutchinson JR, and Shefelbine SJ, "BoneJ: Free and extensible bone image analysis in ImageJ," *Bone*, vol. 47(6), 2020, doi: 10.1016/j.bone.2010.08.023.

[34] "Avizo 2021.1. https://www.fei.com/software/avizo-formaterials-science."

[35] F. F. Lange, "Processing-Related Fracture Origins: I, Observations in Sintered and Isostatically Hot-Pressed A12O3/ZrO2 Composites," *Journal of the American Ceramic Society*, vol. 66, no. 6, pp. 396–398, 1983, doi: 10.1111/j.1151-2916.1983.tb10068.x.

[36] F. F. Lange, B. I. Davis, and I. A. Aksay, "Processing-Related Fracture Origins: III, Differential Sintering of ZrO2 Agglomerates in Al2O3/ZrO2 Composite," *Journal of the American Ceramic Society*, vol. 66, no. 6, pp. 407–408, 1983, doi: 10.1111/j.1151-2916.1983.tb10070.x.

[37] R. Raj and R. K. Bordia, "Sintering behavior of bi-modal powder compacts," *Acta Metallurgica*, vol. 32, pp. 1003-1019, 1984.

[38] G. W. Scherera, “Sintering with Rigid Inclusions,” *Journal of the American Ceramic Society*, vol. 70, no. 10, pp. 719–725, 1987, doi: 10.1111/j.1151-2916.1987.tb04870.x.

[39] C. -L. Fan and M. N. Rahaman, “Factors Controlling the Sintering of Ceramic Particulate Composites: I, Conventional Processing,” *Journal of the American Ceramic Society*, vol. 75, no. 8, pp. 2056–2065, 1992, doi: 10.1111/j.1151-2916.1992.tb04465.x.